Knowledge-Based Systems 188 (2020) 104969

Contents lists available at ScienceDirect

Knowledge-Based Systems

journal homepage: www.elsevier.com/locate/knosys

A new sparse representation framework for compressed sensing MRI☆

Zhen Chen [a,*], Chuanping Huang [b], Shufu Lin [c]

[a] School of Electronic and Information Engineering, South China University of Technology, China
[b] Affiliated Nanfang Hospital, Southern Medical University, China
[c] School of Software, Xiamen University, China

ARTICLE INFO

Article history:
Received 9 April 2019
Received in revised form 2 July 2019
Accepted 15 August 2019
Available online 18 September 2019

Keywords:
Compressed sensing (CS)
Double tight frame (DTF)
Magnetic resonance imaging (MRI)
Robust $L_{1,a}$-norm
Sparse representation (SR)

ABSTRACT

Compressed sensing based Magnetic Resonance imaging (MRI) via sparse representation (or transform) has recently attracted broad interest. The tight frame (TF)-based sparse representation is a promising approach in compressed sensing MRI. However, the conventional TF-based sparse representation is difficult to utilize the sparsity of the whole image. Since the whole image usually has different structure textures and a kind of tight frame can only represent a particular kind of ground object, how to reconstruct high-quality of magnetic resonance (MR) image is a challenge. In this work, we propose a new sparse representation framework, which fuses the double tight frame (DTF) into the mixed-norm regularization for MR image reconstruction from undersampled k-space data. In this framework, MR image is decomposed into smooth and nonsmooth regions. For the smooth regions, the wavelet TF-based weighted L_1-norm regularization is developed to reconstruct piecewise-smooth information of image. For nonsmooth regions, we introduce the curvelet TF-based robust $L_{1,a}$-norm regularization with the parameter to preserve the edge structural details and texture. To estimate the reasonable parameter, an adaptive parameter selection scheme is designed in robust $L_{1,a}$-norm regularization. Experimental results demonstrate that the proposed method can achieve the best image reconstruction results when compared with other existing methods in terms of quantitative metrics and visual effect.

1. Introduction

Magnetic resonance imaging (MRI) has been widely used in clinical diagnosis, since it enables superior visualization of anatomical structure with noninvasive and nonionizing radiation nature [1]. However, the speed of scanning samples in MRI is fundamentally limited by physical and physiological constraints [2]. The recent theory of Compressed Sensing (CS) has been widely utilized to reconstruct Magnetic Resonance (MR) image from a few of undersampled k-space data, if the image is sparse under a given sparse transform [3,4].

Mathematically, The k-space data acquisition model for MR image reconstruction can be modeled as follows:

$$\boldsymbol{y} = \boldsymbol{\Phi x} + \boldsymbol{e} \tag{1}$$

where $\boldsymbol{y} \in \mathbb{C}^M$ denotes the undersampled k-space data, $\boldsymbol{\Phi} \in \mathbb{C}^{M\times N}$ $(M < N)$ is an undersampled Fourier encoding matrix, $\boldsymbol{x} \in \mathbb{C}^N$ is the desired image and $\boldsymbol{e} \in \mathbb{C}^M$ is the noise.

It is well known that the above problem (1) is an ill-posed inverse problem due to under-sampling. To make it well-posed, regularization techniques based on prior information are often explored, such as sparsity [2,5]. The sparsity-based image prior assumes that the image is sparse (or compressible) in sparse transform domain. Thus, the reconstruction process can be modeled by minimizing the regularization function that promotes the sparse solution. It is confirmed that a sparser representation usually leads to lower reconstruction error [6]. To this end, various sparse transforms have been designed, ranging from wavelets, framelets to adaptive transforms [7]. Recently, Tight Frame (TF) is exploited for sparse representation (SR) that leads to an efficient reconstruction result [8], including wavelets [7], shift-invariant wavelets [9], curvelet [10] etc.

In general, each kind of TF-based sparse transform only represents a particular kind of ground object or texture in the sparsity of the whole image, which is inflexible in practical application. For example, the wavelet transform has been well known for sparse representation in image processing community, such as image compression [11], image denoising [12], and image reconstruction [13]. However, the wavelet is usually suitable for dealing with the smooth regions, and are not suitable for discontinuity along a general curve with bounded curvature. MR images often contain curves and edges, wavelet transform may fail in

☆ No author associated with this paper has disclosed any potential or pertinent conflicts which may be perceived to have impending conflict with this work. For full disclosure statements refer to https://doi.org/10.1016/j.knosys.2019.104969.

* Corresponding author.
E-mail address: chenzz@xmu.edu.cn (Z. Chen).

https://doi.org/10.1016/j.knosys.2019.104969
0950-7051/

reconstruction some of edge structural details and texture information [10]. In [10,14], curvelet transform is developed to offer a more optimal performance than wavelets when representing edges of ground objects. Although the data-driven tight frame is proposed and achieving better performance, it is complicated to implement and the high computational overhead [15,16].

Obviously, the existing approaches have limitation in practical application, since the structure of the whole image at different regions are diversification. To enhance the sparse representation, in this paper, a Double Tight Frame (DTF) is developed to construct the sparse representation framework, which is more likely to give a high quality of the reconstructed MR image. In reconstruction processing, MR image is decomposed into two meaningful regions, namely the smooth and the nonsmooth regions. The specific method is to make the sparse representation of wavelet TF in the smooth regions and the sparse representation of curvelet TF in nonsmooth regions, separately.

Once the sparsity is improved by the DTF, another important issue is how to regularize the sparsity in sparse transform domain. The L_0-norm is the most ideal regularization term. However, the L_0-norm minimization is non-convex and NP-hard problem. Although greedy algorithm aims at solving L_0-norm minimization, it often leads to a sub-optimal solution [17]. To tackle this problem, one of the commonly used regularization methods is Tikhonov regularization based on L_2-norm minimization [18]. A common criticism of such regularization method is known to over-smooth edges in the reconstructed result and sensitive to outliers such that it can introduce residual artifacts into reconstructed results [19,20]. In [21], authors used a smoothed L_1-norm regularization to overcome over-smooth edges in a certain sense. Another technique is to use the L_1-norm as a convex relaxation of the L_0-norm [22]. However, the L_1-norm regularization model ignores the structure information of the image [23]. It points out in [24] that the result of the L_1-norm minimization is not sparse enough and reconstructed result generally deviates from the solution we desired. In [25], a non-convex L_p-norm regularization is employed to reconstruct the MR image, which approximates the L_0-norm better than the L_1-norm. However, the L_p-norm ($0 < p < 1$) minimization problem is more difficult to solve than the L_1-norm minimization problem, since it is non-convex and non-smooth. In addition, Zheng et al. [26] pointed out that $p = 1$ outperforms the $p(0 < p < 1)$ value, when the measurement noise is very large or very small. To avoid the difficulty in solving non-convex problem, some weighted L_1-norm ($\mathbf{w}L_1$) regularization are introduced to improve the reconstruction performance [27,28].

More recently, some mixed-norm regularization models have been proposed to overcome above defects [29–31]. In addition, other various techniques have been proposed to improve the reconstruction quality, such as smoothed L_0-norm regularization [32], StructAE [33], low rank matrix approximation [34], $L_{2,1}$-L_1 norm regularization [35] and TV-L_1 norm regularization [36]. Compared with all of the above methods, the mixed-norm regularization method often leads to more accurate reconstruction though at the cost of higher computational complexity. Therefore, a new mixed-norm regularization will be exploited in this paper.

1.1. Contribution

Based upon the above works, we propose a new method for MR image reconstruction, using the DTF-based sparse representation framework with mixed-norm regularization. The DTF-based sparse representation offers a powerful mechanism of combining wavelet sparsity with curvelet sparsity simultaneously. Unlike the previous sparse representation on the whole image, we assume that the image consists of smooth and nonsmooth regions. The wavelet TF and the curvelet TF are applied to the smooth and nonsmooth regions, separately. To improve the reconstruction quality, the mixed-norm regularization model is proposed. For the smooth regions, the weighted L_1-norm with the wavelet TF is employed to reconstruct the piecewise-smooth information of the image. The robust $L_{1,a}$-norm with curvelet TF is used to preserve the edge structural details in the nonsmooth regions. The alternating iterative algorithm is then utilized to solve the proposed optimization problem. Furthermore, an adaptive strategy is introduced to obtain the reasonable parameter in each iteration. Extensive experiments on the MR data demonstrate that the proposed approach attains a significant performance improvement over the existing methods in terms of both quantitative metrics and visual quality.

The rest of the paper is organized as follows: In Section 2, we introduce some basics of CS-based MRI (CS-MRI) and the DTF-based sparse representation that will be used in later sections. In Section 3, the mixed-norm regularization model and its associated algorithm are proposed for MR image reconstruction. Experiment results are shown in Section 4. The conclusion is conducted at the end of the section.

2. Preliminaries

2.1. Conventional CS-MRI

Let $\boldsymbol{x}$ be a $\sqrt{N} \times \sqrt{N}$ MR image in a vector form and it can be represented sparsely in the sparse transform $\boldsymbol{\Psi} \in \mathbb{C}^{L\times N}$. Under this transform, the sparse coefficient $\boldsymbol{\theta} \in \mathbb{C}^L$ can be expressed as $\boldsymbol{\theta} = \boldsymbol{\Psi x}$. A typical CS-MRI problem is to reconstruct an unknown original MR image $\boldsymbol{x}$ from the undersampled k-space data $\boldsymbol{y} \in \mathbb{C}^M$ that is modeled as

$$\min_{\boldsymbol{x}} \frac{1}{2}\|\boldsymbol{y} - \boldsymbol{\Phi x}\|_2^2 + \lambda \boldsymbol{g}(\boldsymbol{\Psi x}), \tag{2}$$

where $\lambda > 0$ is the regularization parameter and $\boldsymbol{g}(\boldsymbol{\Psi x})$ is a regularization term.

As analysis above, one of the key problems for CS-MRI is the choice of sparsity regularization $\boldsymbol{g}(\boldsymbol{\Psi x})$, which can make the underlying image has a perfectly sparse approximation. To improve the reconstruction quality, many works are dedicated to exploiting the sparsity regularization by the sparse prior. Particularly, the TF-based sparse prior is proposed to enhance the performance of image reconstruction.

2.2. Sparse representation with double tight frame

The TF is a kind of sparse transform,[1] and can be employed for the sparse representation of an image. It is confirmed that the design of TF can provide a better sparse approximation to reconstruct MR image [8]. However, conventional TF is to exploit the sparsity of the whole image, so it is not possible to have it both ways, smooth regions and nonsmooth regions. To reconstruct more edge structural details (nonsmooth regions) and offer the piecewise-smooth information (smooth regions) simultaneously, we assume that the reconstructed image $\boldsymbol{x}$ consists of two parts: the smooth regions $\boldsymbol{x}_s$ and the nonsmooth regions $\boldsymbol{x}_n$.

For the smooth regions, the weighted L_1-norm regularization with the wavelet TF-based transform $\boldsymbol{\Psi}_s$ is employed to characterize the piecewise-smooth information. By the TF property, $\boldsymbol{\Psi}_s^H \boldsymbol{\Psi}_s = \boldsymbol{I}$, the sparse coefficient $\boldsymbol{\theta}_s$ can expressed as $\boldsymbol{\theta}_s = \boldsymbol{\Psi}_s \boldsymbol{x}_s$, the weighted L_1-norm regularization model can be rewritten as [38]

$$\boldsymbol{g}_s(\boldsymbol{\theta}_s) = \sum_{i=1}^{L} w(i)|\theta_s(i)|, \tag{3}$$

[1] Tight frame $\boldsymbol{\Psi}^H\boldsymbol{\Psi} = \boldsymbol{I}$, but $\boldsymbol{\Psi}\boldsymbol{\Psi}^H \neq \boldsymbol{I}$ [37].

where $\theta_s(i)$ is ith element of $\boldsymbol{\theta}_s$, the weight $w(i) = \frac{1}{|\theta_s(i)|+\epsilon}$ and $\epsilon > 0$ is a small constant, whose role is to prevent the denominator from reaching zero.

For the nonsmooth regions, we find that the nonsmooth regions of the image often contain edges structural details and textures. Using the weighted L_1-norm model to reconstruct nonsmooth regions will result in over smooth in outline information of the image. To seek the solution, a robust $L_{1,a}$-norm is exploited to preserve the edges structural details and textures. The idea is inspired by the adaptive L_p-norm regularization for different values p. It has been proven that edge regions prefer a lower value p to preserve the detailed information, and smooth regions require a larger value p to avoid artifacts such as staircase effects [39]. Since the L_p-norm model is non-convex, it is difficult to solve it and the value p is difficult to adjust. Taking this into account, we use the curvelet TF-based robust $L_{1,a}$-norm regularization with the parameter a to replace with the adaptive L_p-norm, which can be given as follows

$$\boldsymbol{g}_n(\boldsymbol{\theta}_n) = \frac{1}{a}\sum_{i=1}^{L}\log\big(\cosh(a\theta_n(i))\big), \tag{4}$$

where $\boldsymbol{\theta}_n = \Psi_n\boldsymbol{x}_n$ is the sparse coefficient of $\boldsymbol{x}_n$ under the curvelet TF-based transform Ψ_n, $\theta_n(i)$ is ith element of $\boldsymbol{\theta}_n$ and $a > 0$ is a parameter.

The function $\boldsymbol{g}_n(\boldsymbol{\theta}_n)$ is convex and twice continuously differentiable so that the optimum value can be obtained by the convex optimization algorithm. The corresponding function $\boldsymbol{g}_n(\boldsymbol{\theta}_n)$ and its derivative are shown in Fig. 1. As shown in Fig. 1, for a relatively larger parameter a, the $\boldsymbol{g}_n(\boldsymbol{\theta}_n)$ may close to $L_p(p = 1)$-norm minimization, whereas a smaller parameter a, $\boldsymbol{g}_n(\boldsymbol{\theta}_n)$ may close to $L_p(p = 2)$-norm minimization. Therefore, the robust $L_{1,a}$-norm regularization model has the advantage of the adaptive L_p-norm regularization by adjusting the parameter a. However, how to choose the parameter is a challenge. To overcome this problem, an adaptive strategy will be introduced to obtain the value of parameter in each iteration.

3. The proposed MRI reconstruction framework

In this section, we introduce the proposed sparse representation framework for MR image reconstruction in details. We assume that the image is decomposed into smooth regions and non-smooth regions. The decomposition is automatically realized that we use weighted L_1-norm to reconstruct the smooth regions from the undersampled k-space data. And the residuals are the non-smooth regions that are reconstructed by the robust $L_{1,a}$-norm regularization model. An alternating iteration method is employed to solve the corresponding optimization problem. Furthermore, the parameter a is updated with a closed form in each iteration.

As shown in Fig. 2, we assume $\boldsymbol{x} = \boldsymbol{x}_s + \boldsymbol{x}_n$, where $\boldsymbol{x}_s$ and $\boldsymbol{x}_n$ denote the smooth and nonsmooth regions, separately. Here, the smooth regions are the piecewise-smooth of image without textures and structural details. The residuals are the nonsmooth regions, which mainly consists of edge structural details and textures. Thus, the reconstructed framework of CS-MRI can be formulated as follows

$$\min_{\boldsymbol{x},\boldsymbol{\theta}_s,\boldsymbol{\theta}_n}\frac{1}{2}\|\boldsymbol{y} - \Phi\boldsymbol{x}\|_2^2 + \lambda_s\boldsymbol{g}_s(\boldsymbol{\theta}_s) + \lambda_n\boldsymbol{g}_n(\boldsymbol{\theta}_n), \tag{5}$$

where $\lambda_s, \lambda_n > 0$ are the regularization parameters, the $\boldsymbol{x}_s$ is expressed as $\boldsymbol{x}_s = \Psi_s^H\boldsymbol{\theta}_s$ with respect to Ψ_s and $\boldsymbol{x}_n = \Psi_n^H\boldsymbol{\theta}_n$ with respect to Ψ_n.

Let $\boldsymbol{y} = \begin{bmatrix}\boldsymbol{y}_s\\ \boldsymbol{y}_n\end{bmatrix}$, $\boldsymbol{x} = \begin{bmatrix}\Psi_s^H\boldsymbol{\theta}_s\\ \Psi_n^H\boldsymbol{\theta}_n\end{bmatrix}$, the above optimization problem (5) can be rewritten as:

$$\begin{aligned}\min_{\boldsymbol{\theta}_s,\boldsymbol{\theta}_n}\frac{1}{2}\|\boldsymbol{y}_s - \Phi\Psi_s^H\boldsymbol{\theta}_s\|_2^2 + \lambda_s\boldsymbol{g}_s(\boldsymbol{\theta}_s)\\ + \frac{1}{2}\|\boldsymbol{y}_n + \Phi\Psi_n^H\boldsymbol{\theta}_n\|_2^2 + \lambda_n\boldsymbol{g}_n(\boldsymbol{\theta}_n),\end{aligned} \tag{6}$$

The optimization problem (6) can be solved by following alternative optimizations between $\boldsymbol{\theta}_s$ and $\boldsymbol{\theta}_n$, iteratively.

1. smooth regions: The $\boldsymbol{\theta}_s$ is obtained from the subproblem for the fixed $\boldsymbol{\theta}_n$

$$\min_{\boldsymbol{\theta}_s}\frac{1}{2}\|\boldsymbol{y}_s - \Phi\Psi_s^H\boldsymbol{\theta}_s\|_2^2 + \lambda_s\sum_{i=1}^{L}w(i)|\theta_s(i)|, \tag{7}$$

where $\boldsymbol{y}_s = \boldsymbol{y} - \Phi\Psi_n^H\boldsymbol{\theta}_n$.

Let $\boldsymbol{A}_s = \Phi\Psi_s^H$, its solution can be given by iterative shrinkage-thresholding algorithm [40]

$$\boldsymbol{\theta}_s^{(k+1)} = \boldsymbol{T}_{\lambda_s w}\left(\boldsymbol{\theta}_s^{(k)} - \eta_s\boldsymbol{A}_s^H(\boldsymbol{A}_s\boldsymbol{\theta}_s^{(k)} - \boldsymbol{y}_s^{(k)})\right), \tag{8}$$

where η_s is step-size and the $\boldsymbol{T}_{\lambda_s w}(\boldsymbol{\theta}_s)$ is defined as

$$\boldsymbol{T}_{\lambda_s w}(\boldsymbol{\theta}_s)_i \triangleq \operatorname{sign}(\theta_s(i))\max\big\{|\theta_s(i)| - \lambda_s w(i), 0\big\}$$

and $i = 1, 2, 3, \ldots, L$.

2. nonsmooth regions: Given the fixed $\boldsymbol{\theta}_s$, update the $\boldsymbol{\theta}_n$ via solving the minimization

$$\min_{\boldsymbol{\theta}_n}\frac{1}{2}\|\boldsymbol{y}_n - \Phi\Psi_n^H\boldsymbol{\theta}_n\|_2^2 + \lambda_n\frac{1}{a}\sum_{i=1}^{L}\log\big(\cosh(a\theta_n(i))\big), \tag{9}$$

where $\boldsymbol{y}_n = \boldsymbol{y} - \Phi\Psi_s^H\boldsymbol{\theta}_s$.

Let $h(\boldsymbol{\theta}_n) = \log(\cosh(a\boldsymbol{\theta}_n))$, then $h(\boldsymbol{\theta}_n)$ can be approximated by first-order Taylor expansion

$$h(\boldsymbol{\theta}_n) = h\left(\boldsymbol{\theta}_n^{(k)}\right) + \left\langle\nabla h(\boldsymbol{\theta}_n^{(k)}), \boldsymbol{\theta}_n - \boldsymbol{\theta}_n^{(k)}\right\rangle, \tag{10}$$

where $\boldsymbol{\theta}_n^{(k)}$ is the solution obtained at the kth iteration.

After ignoring constant terms in Eq. (10), the minimization problem (9) can be solved by iteratively

$$\min_{\boldsymbol{\theta}_n}\frac{1}{2}\|\boldsymbol{y}_n - \Phi\Psi_n^H\boldsymbol{\theta}_n\|_2^2 + \lambda_n\left\langle\tanh(a\boldsymbol{\theta}_n^{(k)}), \boldsymbol{\theta}_n\right\rangle, \tag{11}$$

Using the Karush-Kuhn-Tucher (KKT) condition, the derivative of the minimization subproblem (11) can be solved as

$$\boldsymbol{\theta}_n^{(k+1)} = \left(\boldsymbol{A}_n^H\boldsymbol{A}_n\right)^{-1}\left(\boldsymbol{A}_n^H\boldsymbol{y}_n^{(k)} + \lambda_n\tanh(a\boldsymbol{\theta}_n^{(k)})\right), \tag{12}$$

where $\boldsymbol{A}_n = \Phi\Psi_n^H$ and $(\boldsymbol{A}_n^H\boldsymbol{A}_n)^{-1}$ can be calculated ahead, making above computation more effective.

3.1. Choice of the parameter a

Note that the parameter a in (9) might not be the best choice for MR image reconstruction problem. To make our method more competitive, we propose an adaptive strategy to obtain the parameter value, which can successfully preserve the detailed information and avoid artifacts. For expression convenience, we rewrite $\sum_{i=1}^{L}\log(\cosh(a\theta_n(i)))$ as $\log(\cosh(a\theta_n))$. Accordingly, the minimization problem (9) can be rewritten as

$$\min_{\boldsymbol{\theta}_n}\frac{1}{2}\|\boldsymbol{y}_n - \boldsymbol{A}_n\boldsymbol{\theta}_n\|_2^2 + \lambda_n\frac{1}{a}\log\big(\cosh(a\boldsymbol{\theta}_n)\big), \tag{13}$$

Thus, we set the derivative of (13) with respect to $\boldsymbol{\theta}_n^{(k)}$ equal to zero. That is

$$a^{(k)}\boldsymbol{\theta}_n^{(k)} = \operatorname{arctanh}\big(\frac{1}{\lambda_n}\boldsymbol{A}_n^H(\boldsymbol{A}_n\boldsymbol{\theta}_n^{(k)} - \boldsymbol{y}_n^{(k)})\big) \tag{14}$$

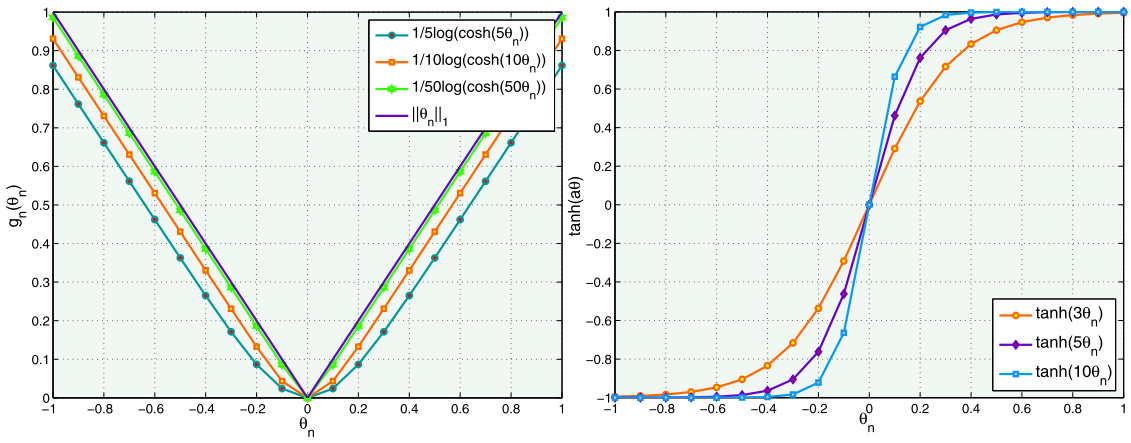

Fig. 1. Left: illustrations of the regularization function $\boldsymbol{g}_n(\boldsymbol{\theta}_n(i)) = \frac{1}{a}\log(\cosh(a\theta_n(i)))$. Right: the derived function $\boldsymbol{g}_n'(\theta_n(i)) = \tanh(a\theta_n(i))$ with different value a.

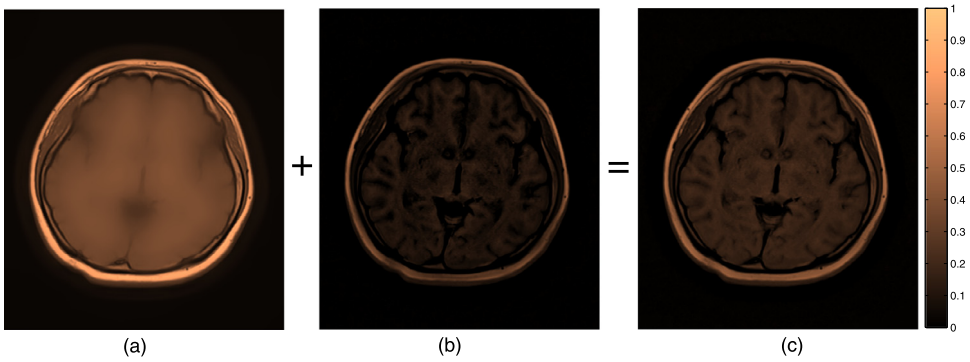

Fig. 2. Structure decomposition of MR image. (a) smooth regions; (b) nonsmooth regions.

Taking the L_2-norm of both sides of (14) gives rise to

$$a^{(k)}\left\|\boldsymbol{\theta}_n^{(k)}\right\|_2 = \left\|\operatorname{arctanh}\left(\frac{1}{\lambda_n}\boldsymbol{A}_n^H(\boldsymbol{A}_n\boldsymbol{\theta}_n^{(k)} - \boldsymbol{y}_n^{(k)})\right)\right\|_2 \tag{15}$$

Thus the estimated regularization parameter $a^{(k)}$ is given by

$$a^{(k)} = \frac{\left\|\operatorname{arctanh}\left(\frac{1}{\lambda_n}\boldsymbol{A}_n^H(\boldsymbol{A}_n\boldsymbol{\theta}_n^{(k)} - \boldsymbol{y}_n^{(k)})\right)\right\|_2}{\left\|\boldsymbol{\theta}_n^{(k)}\right\|_2 + \epsilon} \tag{16}$$

where $\epsilon > 0$ is a small constant, whose role is to prevent the denominator from reaching zero. It is clear that the parameter $a^{(k)}$ can be updated adaptively during the iterations.

The proposed algorithm is listed as follows.

Algorithm 1 The DTF-based sparse representation for CS-MRI (DTF-MRI)

1: **Initialization**: Set $\boldsymbol{y}$, wavelet tight frame Ψ_n, curvelet tight frame Ψ_s, λ_n, λ_s, $a^{(0)}$; undersampled matrix Φ; $\boldsymbol{\theta}_n^{(0)} = \Psi_n\Phi^H\boldsymbol{y}$,
2: **While:** the stopping criterion is not met **do**
3: For smooth regions:
4: Estimate $\boldsymbol{y}_s$: $\boldsymbol{y}_s^{(k)} = \boldsymbol{y} - \boldsymbol{A}_n\boldsymbol{\theta}_n^{(k)}$;
5: Update $\boldsymbol{\theta}_s^{(k+1)}$ by computing Eq. (8);
6: For nonsmooth regions:
7: Estimate $\boldsymbol{y}_n$: $\boldsymbol{y}_n^{(k)} = \boldsymbol{y} - \boldsymbol{A}_s\boldsymbol{\theta}_s^{(k+1)}$;
8: Update $\boldsymbol{\theta}_n^{(k+1)}$ by computing Eq. (12);
9: Update the parameter $a^{(k)}$ by computing Eq. (16);
10: **end while**
11: $\boldsymbol{x}^{(k+1)} = \Psi_s^H\boldsymbol{\theta}_s^{(k+1)} + \Psi_n^H\boldsymbol{\theta}_n^{(k+1)}$;
12: **Output** $\hat{\boldsymbol{x}}$

4. Numerical experiments

To validate the effectiveness of the proposed method, we conduct a set of MR data for reconstruction applications. The first presents the implementation details and some quantitative indices are provided to measure the quality of image reconstruction. We test the proposed method over MR images with different features including the reconstruction errors, sampling patterns/ratios and noise levels. The proposed method will be shown to have better performance in comparison with some existing methods, such as NNM-MRI [41], pFISTA [8] and FTVNNR [42]. The implementation of above methods are obtained from their authors' website. To be fair, the counterparts used in the comparisons are obtained with the best performances via careful adjustment of their parameters in the algorithms. The regularization parameters λ_s and λ_n are set as 0.001 and 0.3. The experiments are performed on MATLAB on PC with Intel Core i3 processor, 8G RAM and Microsoft Windows 7 operation system.

For quantitative comparison of the reconstructed results, the relative L_2 norm error (RLNE) is used to depict the difference between the reconstructed image and the original image. Generally speaking, the smaller the RLNE value, the better the image reconstruction quality. It is defined as

$$\text{RLNE} \triangleq \frac{\|\hat{\boldsymbol{x}} - \boldsymbol{x}\|_2}{\|\boldsymbol{x}\|_2} \tag{17}$$

where $\boldsymbol{x}$ is the original image, while $\hat{\boldsymbol{x}}$ is the reconstructed image.

We also use the Structure Similarity Index Measure (SSIM), which is good at measuring quality of the reconstructed image in terms of image structure [43]. More formally, SSIM is given by

$$\text{SSIM}(a, b) \triangleq \frac{(2\mu_a\mu_b + C_1)(2\sigma_{ab} + C_2)}{(\mu_a^2 + \mu_b^2 + C_1)(\sigma_a^2 + \sigma_b^2 + C_2)}, \tag{18}$$

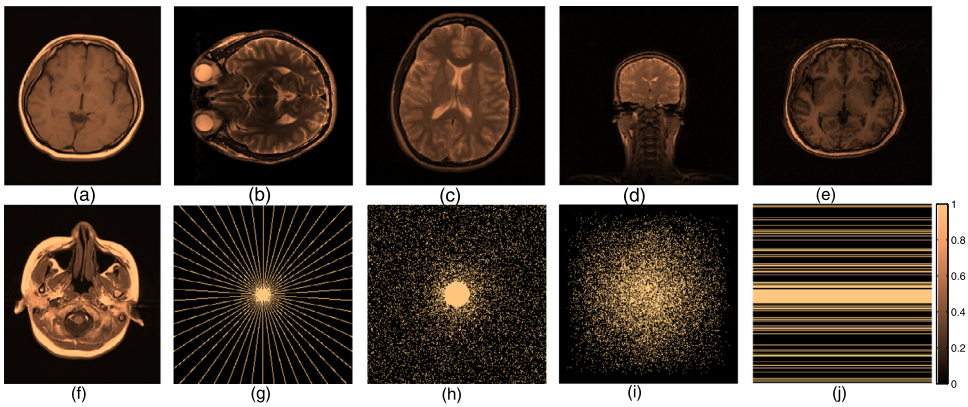

Fig. 3. Gold standard images used in the experiment. (a)–(f) MRI1, MRI2, MRI3, MRI4, MRI5 and MRI6. (g)–(j) sampling pattern: radial, Circle, random and Cartesian sampling.

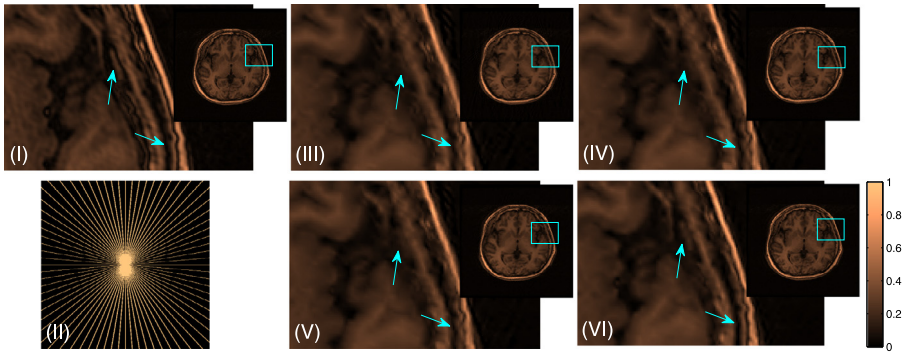

Fig. 4. Reconstructed MR image (MRI5) under the noiseless case. (I) is the original image and (II) is the radial sampling pattern. (III)-(VI) are the reconstructed results using NNM-MRI, pFISTA, FTVNNR and the proposed method, respectively.

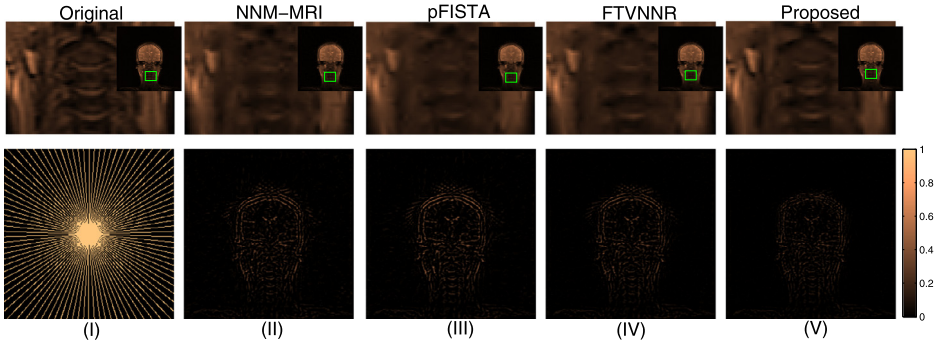

Fig. 5. Reconstructed MR image (MRI4) under the noiseless case. (I) Above is the original image and below is the radial sampling pattern. (II)–(V) Above are the reconstructed results using NNM-MRI, pFISTA, FTVNNR and the proposed method, respectively; below are the corresponding reconstruction errors.

where μ_a is the mean intensity of a; μ_b is the mean intensity of b; σ_a^2 is the variance of a; and σ_b^2 is the variance of b. Constants C_1 and C_2 are used to avoid instabilities when the denominator is very close to zero. A large value of SSIM indicates that the two images are highly similar in the structure. It means that the details of the original image are preserved. In addition, Signal-to-Noise Ratio (SNR) is used for result evaluation:

$$\mathrm{SNR} \triangleq 10 \log_{10} \left(\frac{B_{\mathrm{Var}}}{A_{\mathrm{Mean}}} \right), \tag{19}$$

where A_{Mean} is the mean square error between the original image $\boldsymbol{x}$ and the reconstructed image $\hat{\boldsymbol{x}}$, B_{Var} denotes the variance of the original image $\boldsymbol{x}$. The test images used in our experiments are shown in Fig. 3.

4.0.1. Comparison on visual quality

In order to demonstrate the superiority of proposed method, the reconstruction qualities are evaluated from visual inspection. Figs. 5–6 exhibit reconstructed results of the MR image and corresponding reconstructed errors. For a visual comparison, we magnify the same detail region of reconstructed results. As shown in Figs. 4 and 7, the visible artifacts can be observed on the reconstructed image by NNM-MRI. The quality of the reconstructed images by using pFISTA, FTVNNR are better than that of NNM-MRI, but they still loses some subtle information that degrade clearness of edge contour structure. All of these methods deal with the image as a whole, which is difficult to seek a tradeoff between the preservation of edge structural details in the nonsmooth regions and the avoidance of staircase effects in the smooth regions. We utilize the DTF-based regularization

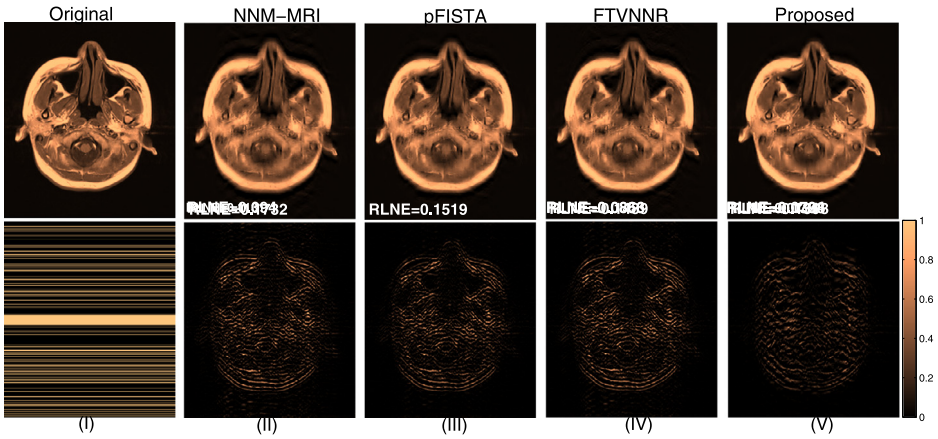

Fig. 6. Reconstructed MR image (MRI6) under the noiseless case. (I) Above is the original image and below is the Cartesian sampling pattern. (II)–(V) Above are the reconstructed results using NNM-MRI, pFISTA, FTVNNR and the proposed method, respectively; below are the corresponding reconstruction errors.

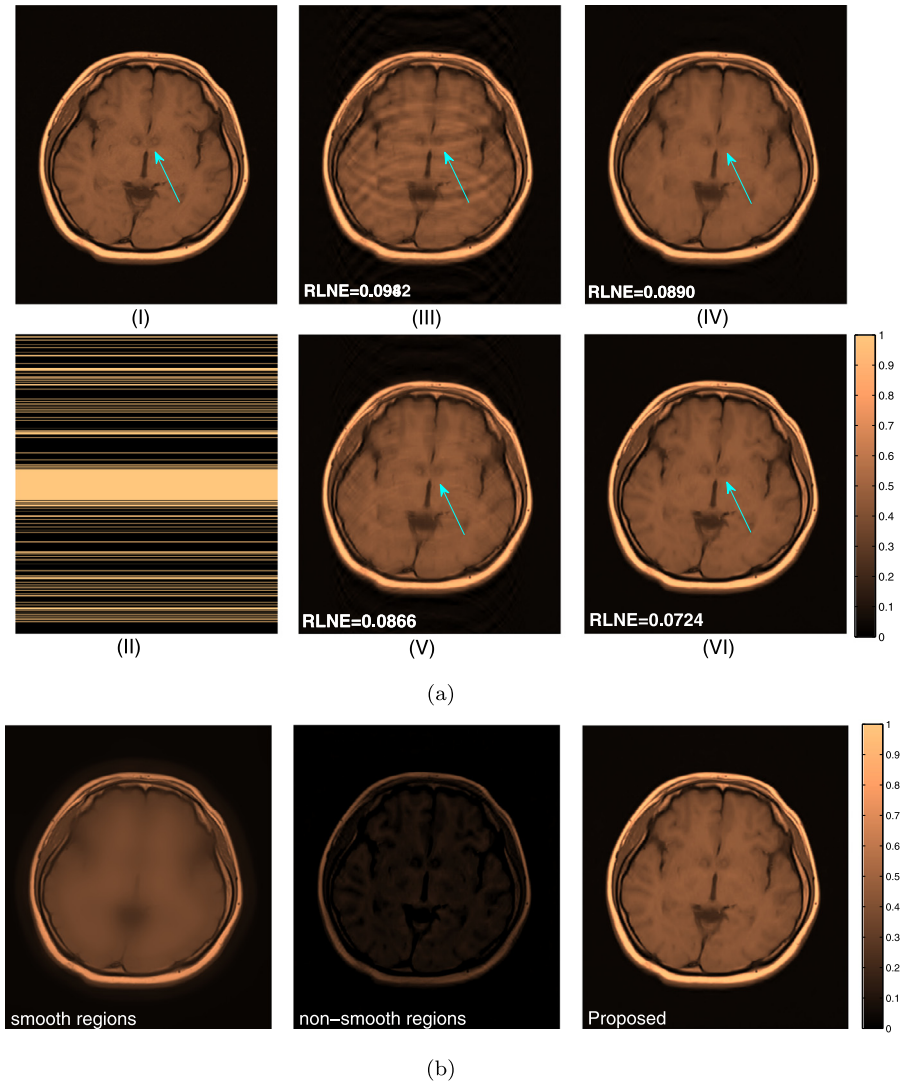

Fig. 7. Reconstructed MR image (MRI1) after the ablation surgery under the noiseless case. (a): (I) is the original image and (II) is the Cartesian sampling pattern. (III)–(VI) are the reconstructed results using NNM-MRI, pFISTA, FTVNNR and the proposed method, respectively. (b): Left is the result of smooth regions, middle is the result of nonsmooth regions and right is the final result.

terms to deal with the smooth and nonsmooth regions separately, in which some of subtle edges texture are better preserved, and the image sharpness is improved significantly.

To show the effects of the DTF-based regularization terms, the smooth and nonsmooth regions obtained by our method are shown in Fig. 7(b). The results show that the most of structure

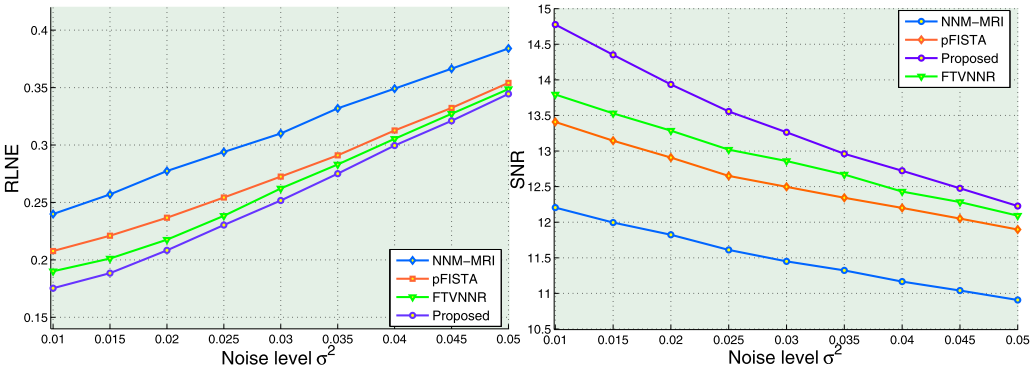

Fig. 8. Left: The RLNEs versus noise level σ^2. Right: SNRs versus noise level σ^2.

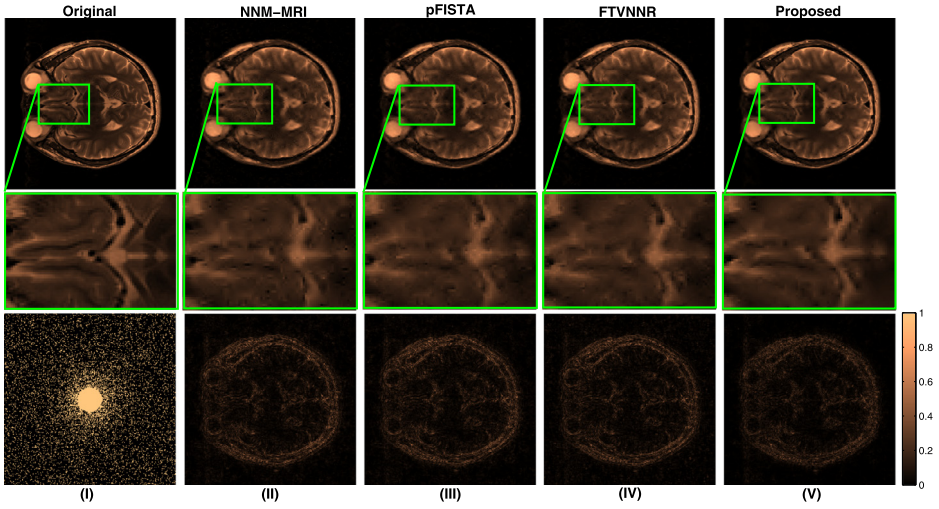

Fig. 9. Reconstructed T2 brain image under the noise case ($\sigma^2 = 0.02$). (I) Above is the original image; middle is the partial enlargement of the original image and below is the Circle sampling pattern. (II)–(V) Above are the reconstructed images using NNM-MRI, pFISTA, FTVNNR and the proposed method, respectively; middle are the corresponding partial enlargement of the reconstructed results and below are the corresponding reconstruction errors.

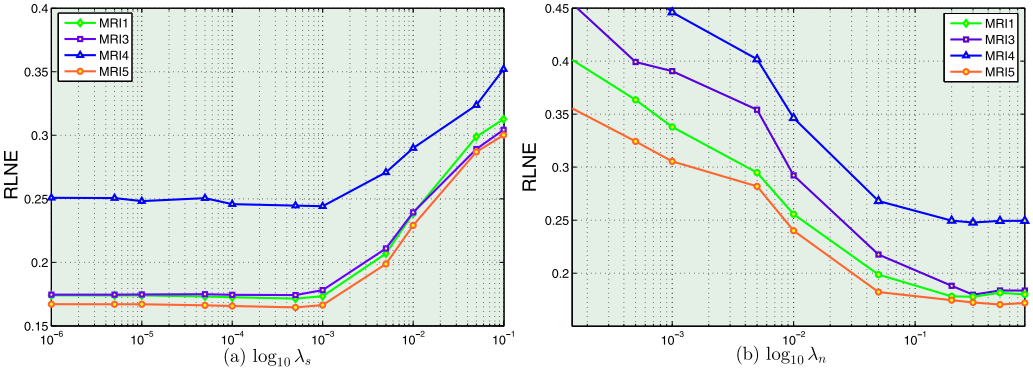

Fig. 10. Left: RLNEs versus the parameters λ_s (fixed $\lambda_n = 0.3$). Right: RLNEs versus the parameters λ_n (fixed $\lambda_s = 10^{-3}$).

in image can be reconstructed by the weighted L_1-norm regularization method, but there are loss of edge structural details and textures. Therefore the robust $L_{1,a}$-norm regularization is helpful to improve the reconstructed results. In Fig. 7, we further address the MR image reconstruction after the ablation surgery, which are associated with nucleus accumbens lesion. As can be seen in Fig. 7, the peripheral edema after the operation can be discerned by the proposed method, while the other methods are difficult to obtain clear identification.

In order to further illustrate the superiority of the proposed method, we show quantitative comparisons of the different methods. The RLNE, SSIM and SNR of the reconstructed MR images with 18% sampling ratio are given in Table 1. MRI3, MRI4 and MRI6 are test images used in Fig. 3. Clearly, the proposed method achieves the lowest RLNE index and the highest SSIM and SNR. This comparisons show the superior reconstruction ability of the proposed method. It further confirms the effectiveness of the proposed method, which is beneficial in clinical diagnosis.

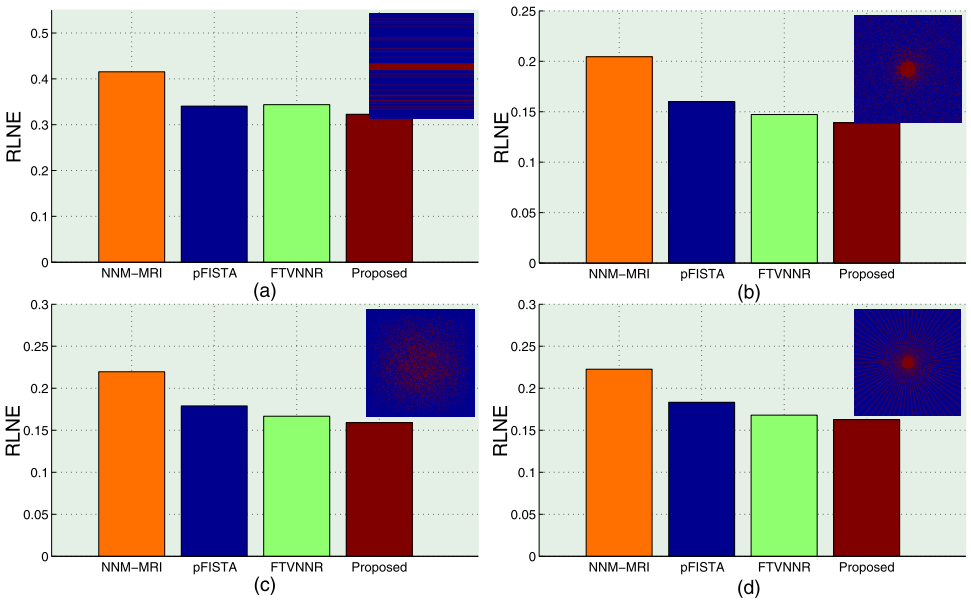

Fig. 11. RLNEs versus sampling patterns with the 15% sampling ratios. (a)–(d) Sampling patterns: Cartesian, Circle, random and radial sampling.

Table 1
Comparison of MR image reconstruction with different methods for test images in Fig. 3.

Methods	MRI3			MRI4			MRI6		
	RLNE	SSIM	SNR	RLNE	SSIM	SNR	RLNE	SSIM	SNR
NNM-MRI	0.264	0.9920	12.56	0.220	0.9799	12.12	0.222	0.9211	11.27
pFISTA	0.254	0.9901	12.82	0.205	0.9831	12.85	0.211	0.9306	11.72
FTVNNR	0.255	0.9902	12.92	0.195	0.9856	13.12	0.208	0.9354	12.25
Proposed	0.242	0.9961	14.64	0.183	0.9946	15.02	0.192	0.9433	14.58

4.0.2. Comparison on the noise case

For practical consideration, we conduct experiments on sampled data polluted by different noise levels to evaluate the performance of the proposed method. In the experiments, Gaussian noise is added to the real and imaginary parts of sampled data. The noise variance is set from 0.01 to 0.05 respectively. In Fig. 8, the performance reduces when noise level increases, while the proposed DTF-MRI still achieves best results than all competing methods.

To reflect the qualitative nature of reconstruction in noise case, the reconstructed results together with the corresponding errors are shown in Fig. 9. It is easy to see that the results obtained with other methods are both noisy and blurry. The result obtained with our method is relatively clear. Compared with the reconstruction errors, we can conclude that the proposed method is still superior to that of the competing methods in the noise case.

4.0.3. Discussions of the regularization parameters

In this subsection, we discuss how to select the best regularization parameters, λ_s, λ_n, for the performance of the proposed DTF-MRI method. For these two parameters, FTVNNR set $\lambda_s = 0.01$ and $\lambda_n = 1$ empirically. However, if λ_s and λ_n are determined in an appropriate manner, this may yield a better reconstruction effect. To investigate the sensitivity of our method against λ_s, λ_n, two experiments are conducted with respect to different λ_s, λ_n in Fig. 10.

The first experiment verifies that the reconstructed performance is influenced by different values λ_s and the fixed parameter $\lambda_n = 0.3$. As shown in Fig. 10(left), it is found that the performance of the proposed method is less affected, if the parameter λ_s is smaller than 0.001. Therefore, in this work λ_s is empirically set to be $\lambda_s = 0.001$. We also conduct the experiments with the fixed parameter $\lambda_s = 0.001$ under variable λ_n in Fig. 10(right). We can see that the RLNE varies slightly if λ_n is in the range of 0.3 to 1. To this end, the regularization parameters λ_s and λ_n are set as 0.001 and 0.3 for MRI reconstruction.

4.0.4. Reconstruction with different sampling patterns

In this subsection, the different sampling patterns are considered to demonstrate the performance of the proposed method. The RLNE index of all methods under different sampling patterns can be found in Fig. 11. As a result, we see that our method consistently outperforms all other approaches for all sampling patterns in terms of RLNE index, which implies that the advantages of the proposed method are not change under the different sampling patterns.

4.0.5. Convergence of the proposed algorithm

To demonstrate the effectiveness and applicability of our method, the convergence of the proposed method is empirically conducted in Fig. 12. All of test images are given in Fig. 3. Fig. 12 illustrates the convergent performance of the proposed DTF-MRI in the noiseless and noise cases, respectively. It is observed that with the increasing of iteration number, all of the RLNE curves decrease gradually and ultimately become flat and stable. It implies that the proposed method has a good astringency.

4.0.6. Reconstruction with sampling ratios

In this subsection, we evaluate the performance of the proposed method using the different undersampling ratios. Fig. 13 depicts the RLNE/SNR curves as a function of sampling ratios for the different methods. It is obvious that the proposed method outperforms all competing methods under the different sampling ratios on both RLNE and SNR index.

From the left of Fig. 13, it is seen that the reconstructed quality obtained by the proposed method with 30% sampling, while FTVNNR requires 44% sampling and the others need more sampling. It is also observed that the RLNE index of proposed method is gradually close to that of FTVNNR, with the sampling ratios increasing. It implies that the proposed method is more effective for MR image reconstruction in the low sampling ratios case.

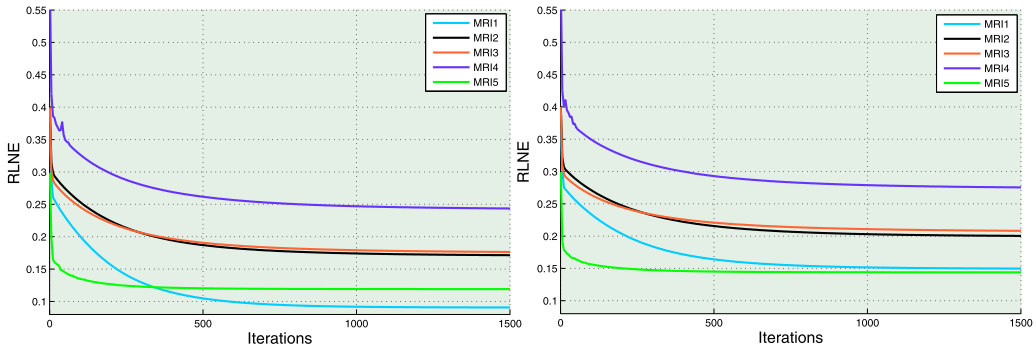

Fig. 12. The convergence of the proposed algorithm. Progression of the RLNE results achieved by proposed method for test images with respect to the iteration number, under the noiseless (left) and noise (right) case (noise variance $\sigma^2 = 0.02$).

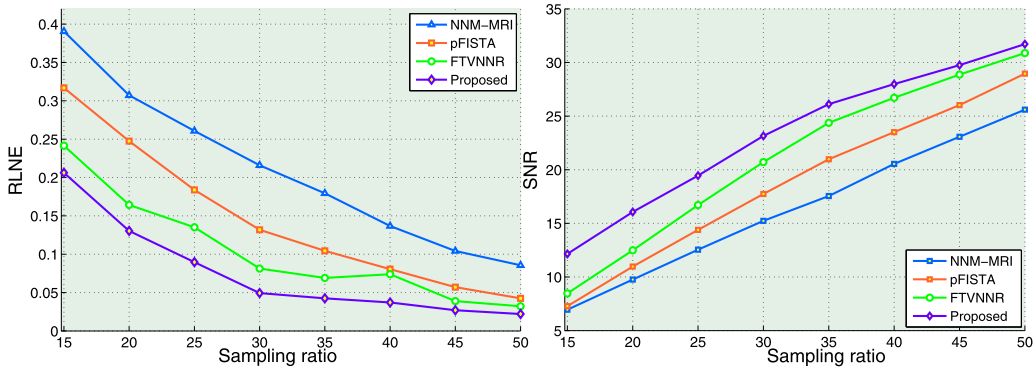

Fig. 13. Left: The RLNEs versus sampling ratios. Right: SNRs versus sampling ratios.

5. Conclusion

This paper presented a new sparse representation framework for the application of CS-MRI. The proposed method employed two kinds of TF-based transform to establish a mixed-norm regularization model, which can exploit the advantage of the wavelet TF-based transform and curvelet TF-based transform domain, simultaneously. The solution of the proposed method was given by the alternating iterative algorithm. The key point is to combine DTF-based sparse representation with a new mixed regularization model together, which preserve the edge structural details in nonsmooth regions and piecewise-smooth information of image in smooth regions, separately. Various experimental results demonstrate that the proposed DTF-MRI can achieve the superior performance in detail clarity and noise suppression from the objective and subjective visual evaluation.

Acknowledgments

The authors would like to thank the anonymous reviewers for their comments and suggestions. This work was supported by youth visiting scholar program of Chinese Ministry of Education.

References

[1] R.A. Zoroofi, Y. Sato, S. Tamura, H. Naito, An improved method for MRI artifact correction due to translational motion in the imaging plane, IEEE Trans. Med. Imaging 14 (3) (1995) 471–479.
[2] J. Duan, Y. Liu, L. Zhang, Bregman iteration based efficient algorithm for MR image reconstruction from undersampled *k*-space data, IEEE Signal Process. Lett. 20 (8) (2013) 831–834.
[3] X. Fan, Q. Lian, B. Shi, Compressed-sensing MRI based on adaptive tight frame in gradient domain, Appl. Mag. Reson. 49 (5) (2018) 465–477.
[4] M. Lustig, D. Donoho, J.M. Pauly, Sparse MRI: The application of compressed sensing for rapid MR imaging, Mag. Reson. Med. 58 (6) (2007) 1182–1195.
[5] Y. Quan, H. Ji, Z. Shen, Data-driven multi-scale non-local wavelet frame construction and image recovery, J. Sci. Comput. 63 (2) (2015) 307–329.
[6] S. Ravishankar, Y. Bresler, MR image reconstruction from highly undersampled *k*-space data by dictionary learning, IEEE Trans. Med. Imaging 30 (5) (2011) 1028–1041.
[7] C. Bao, H. Ji, Z. Shen, Convergence analysis for iterative data-driven tight frame construction scheme, Appl. Comput. Harmon. Anal. 38 (3) (2015) 510–523.
[8] Y. Liu, Z. Zhan, J.-F. Cai, D. Guo, Z. Chen, X. Qu, Projected iterative soft-thresholding algorithm for tight frames in compressed sensing magnetic resonance imaging, IEEE Trans. Med. Imaging 35 (9) (2016) 2130–2140.
[9] R.R. Coifman, D.L. Donoho, Translation-invariant de-noising, in: Wavelets and Statistics, Springer, 1995, pp. 125–150.
[10] E. Candès, L. Demanet, D. Donoho, L. Ying, Fast discrete curvelet transforms, Multiscale Model. Simul. 5 (3) (2006) 861–899.
[11] F. Li, L. Xin, Y. Guo, J. Gao, X. Jia, A framework of mixed sparse representations for remote sensing images, IEEE Trans. Geosci. Remote Sens. 55 (2) (2017) 1210–1221.
[12] S.G. Chang, B. Yu, M. Vetterli, Adaptive wavelet thresholding for image denoising and compression., IEEE Trans. Image Process. 9 (9) (2002) 1532–1546.
[13] M. Belge, M.E. Kilmer, E.L. Miller, Wavelet domain image restoration with adaptive edge-preserving regularization, IEEE Trans. Image Process. 9 (4) (2000) 597–608.
[14] J.-L. Starck, E.J. Candès, D.L. Donoho, The curvelet transform for image denoising, IEEE Trans. Image Process. 11 (6) (2002) 670–684.
[15] J.F. Cai, H. Ji, Z. Shen, G.B. Ye, Data-driven tight frame construction and image denoising, Appl. Comput. Harmon. Anal. 37 (1) (2014) 89–105.
[16] Z. Zhan, J.-F. Cai, D. Guo, Y. Liu, Z. Chen, X. Qu, Fast multiclass dictionaries learning with geometrical directions in MRI reconstruction, IEEE Trans. Biomed. Eng. 63 (9) (2016) 1850–1861.
[17] D. Li, Q. Wang, Y. Shen, Intelligent greedy pursuit model for sparse reconstruction based on ℓ_0 minimization, Signal Process. 122 (2016) 138–151.
[18] X. Zhang, E.Y. Lam, E.X. Wu, K.K. Wong, Application of Tikhonov Regularization to Super-Resolution Reconstruction of Brain MRI Images, in: Medical Imaging and Informatics, 2008, pp. 51–56.
[19] M. Storath, C. Brandt, M. Hofmann, T. Knopp, J. Salamon, A. Weber, A. Weinmann, Edge preserving and noise reducing reconstruction for magnetic particle imaging, IEEE Trans. Med. Imaging 36 (1) (2017) 74–85.

[20] X. Liu, L. Chen, W. Wang, J. Zhao, Robust multi-frame super-resolution based on spatially weighted half-quadratic estimation and adaptive BTV regularization, IEEE Trans. Image Process. 27 (10) (2018) 4971–4986.
[21] I. Onaran, N.F. Ince, A.E. Cetin, Sparse spatial filter via a novel objective function minimization with ℓ_1-norm regularization, Biomed. Signal Process. Control 8 (3) (2013) 282–288.
[22] D.L. Donoho, Compressed sensing, IEEE Trans. Inf. Theory 52 (4) (2006) 1289–1306.
[23] S. Liu, J. Zhang, J. Liu, Q. Yin, $\ell_{1/2,1}$ Group sparse regularization for compressive sensing, Signal Image Video Process. 10 (5) (2016) 1–8.
[24] X. Huang, Y. Liu, L. Shi, S.V. Huffel, J.A.K. Suykens, Two-level ℓ_1 minimization for compressed sensing, Signal Process. 108 (2015) 459–475.
[25] H. Song, L. Qing, Y. Wu, X. He, Adaptive regularization-based space–time super-resolution reconstruction, Signal Process. Image Commun. 28 (7) (2013) 763–778.
[26] L. Zheng, A. Maleki, H. Weng, X. Wang, T. Long, Does ℓ_p-minimization outperform ℓ_1-minimization?, IEEE Trans. Inform. Theory 63 (11) (2017) 6896–6935.
[27] C.-D. Pan, L. Yu, H.-L. Liu, Z.-P. Chen, W.-F. Luo, Moving force identification based on redundant concatenated dictionary and weighted ℓ_1-norm regularization, Mech. Syst. Signal Process. 98 (2018) 32–49.
[28] H. Kim, J. Chen, A. Wang, C. Chuang, M. Held, J. Pouliot, Non-local total-variation (NLTV) minimization combined with reweighted ℓ_1-norm for compressed sensing CT reconstruction, Phys. Med. Biol. 61 (18) (2016) 6878–6891.
[29] Y. Shen, B. Han, E. Braverman, Stability of the elastic net estimator, J. Complexity 32 (1) (2015) 20–39.
[30] S. Bengio, F. Pereira, Y. Singer, D. Strelow, Group sparse coding, Adv. Neural Inf. Process. Syst. 22 (11) (2009) 82–89.
[31] E. Chouzenoux, A. Jezierska, J.-C. Pesquet, H. Talbot, A majorize-minimize subspace approach for ℓ_2-ℓ_0 image regularization, SIAM J. Imaging Sci. 6 (1) (2013) 563–591.
[32] X. Qu, X. Cao, D. Guo, C. Hu, Z. Chen, Compressed sensing MRI with combined sparsifying transforms and smoothed ℓ_0 norm minimization, in: Acoustics Speech and Signal Processing (ICASSP), 2010 IEEE International Conference on, IEEE, 2010, pp. 626–629.
[33] X. Peng, J. Feng, S. Xiao, W.Y. Yau, S. Yang, Structured autoencoders for subspace clustering, IEEE Trans. Image Process. 27 (10) (2018) 5076–5086.
[34] X. Peng, C. Lu, Z. Yi, H. Tang, Connections between nuclear-norm and frobenius-norm-based representations, IEEE Trans. Neural Netw. Learn. Syst. 29 (1) (2016) 218–224.
[35] A. Gramfort, D. Strohmeier, J. Haueisen, M.S. Hämäläinen, M. Kowalski, Time-frequency mixed-norm estimates: Sparse M/EEG imaging with non-stationary source activations, Neuroimage 70 (2) (2013) 410–422.
[36] F. Xiaoyu, L. Qiusheng, S. Baoshun, Compressed sensing MRI with phase noise disturbance based on adaptive tight frame and total variation, IEEE Access 5 (2017) 19311–19321.
[37] A. Majumdar, R.K. Ward, On the choice of compressed sensing priors and sparsifying transforms for MR image reconstruction: An experimental study, Signal Process. Image Commun. 27 (9) (2012) 1035–1048.
[38] E.J. Candès, M.B. Wakin, S.P. Boyd, Enhancing sparsity by reweighted ℓ_1 minimization, J. Fourier Anal. Appl. 14 (5–6) (2008) 877–905.
[39] H. Shen, L. Peng, L. Yue, Q. Yuan, L. Zhang, Adaptive norm selection for regularized image restoration and super-resolution, IEEE Trans. Cybern. 46 (6) (2017) 1388–1399.
[40] A. Beck, M. Teboulle, A fast iterative shrinkage-thresholding algorithm for linear inverse problems, SIAM J. Imaging Sci. 2 (1) (2009) 183–202.
[41] A. Majumdar, R.K. Ward, Causal dynamic MRI reconstruction via nuclear norm minimization, Mag. Reson. Imaging 30 (10) (2012) 1483–1494.
[42] J. Yao, Z. Xu, X. Huang, J. Huang, An efficient algorithm for dynamic MRI using low-rank and total variation regularizations, Med. Image Anal. 44 (2018) 14–27.
[43] Z. Wang, A.C. Bovik, H.R. Sheikh, E.P. Simoncelli, Image quality assessment: from error visibility to structural similarity, IEEE Trans. Image Process. 13 (4) (2004) 600–612.